

# CrystEngComm

Accepted Manuscript



This is an *Accepted Manuscript*, which has been through the Royal Society of Chemistry peer review process and has been accepted for publication.

*Accepted Manuscripts* are published online shortly after acceptance, before technical editing, formatting and proof reading. Using this free service, authors can make their results available to the community, in citable form, before we publish the edited article. We will replace this *Accepted Manuscript* with the edited and formatted *Advance Article* as soon as it is available.

You can find more information about *Accepted Manuscripts* in the [Information for Authors](#).

Please note that technical editing may introduce minor changes to the text and/or graphics, which may alter content. The journal's standard [Terms & Conditions](#) and the [Ethical guidelines](#) still apply. In no event shall the Royal Society of Chemistry be held responsible for any errors or omissions in this *Accepted Manuscript* or any consequences arising from the use of any information it contains.

## COMMUNICATION

## Rapid and Facile One-Step Synthesis of LiTaO<sub>3</sub> Nanorods

Cite this: DOI: 10.1039/x0xx00000x

P.W. Jaschin and K.B.R. Varma\*

Received 00th January 2012,  
Accepted 00th January 2012

DOI: 10.1039/x0xx00000x

www.rsc.org/

**Single crystalline LiTaO<sub>3</sub> nanorods (length of 2.5–6 μm and a diameter of 200–500 nm) were synthesized via a facile molten-salt technique. An individual single crystalline nanorod exhibited a piezoelectric coefficient of 8 pm/V. An improved optical frequency-doubling efficiency was observed in the case of LiTaO<sub>3</sub> nanorods as compared to that of cubic crystallites of similar size.**

One-dimensional nanostructures of various functional oxides find multiple applications in nanoscale actuators and sensors,<sup>1,2</sup> electromechanical and nano-generator-based energy harvesting systems.<sup>3–9</sup> Perovskite-based ternary metal oxides, in particular, provide a better platform for such applications considering their unique ferroelectric, piezoelectric, electrostrictive, magnetic, non-linear optic and photocatalytic behavior.<sup>10–15</sup> It has been recognized that dimensional confinement can induce intriguing properties distinct from that of bulk materials. Literature is replete with reports on the synthesis and characterization of one-dimensional mono-crystalline perovskite oxides such as BaTiO<sub>3</sub>,<sup>16</sup> SrTiO<sub>3</sub>,<sup>16</sup> BiFeO<sub>3</sub>,<sup>13</sup> LiNbO<sub>3</sub><sup>17</sup> and KNbO<sub>3</sub>.<sup>18</sup> Hydrothermal synthesis, template-assisted crystal growth and molten-salt synthesis are three major techniques employed to induce anisotropic growth in nanostructures. Amongst these, molten-salt synthesis presents a more facile and less time-consuming method for accomplishing oriented or anisotropic crystal growth.

Lithium tantalate (LiTaO<sub>3</sub>), an exceptional multifunctional material, has been extensively exploited for piezoelectric (piezoelectric coefficient,  $d_{33} = 8$  pC/N),<sup>19</sup> pyroelectric (pyroelectric coefficient,  $p = 23$  nC/cm<sup>2</sup>K)<sup>20</sup> and ferroelectric device (remnant polarization,  $P_r = 50$  μC/cm<sup>2</sup>)<sup>21</sup> applications. It has a rhombohedral structure with a space group of  $R\bar{3}c$  and

undergoes a ferroelectric-to-paraelectric transition (associated with the space group  $R\bar{3}c$ ) around 620°C.<sup>22</sup> It is one of the most prominent photorefractive materials with a large non-linear<sup>22</sup> and electro-optic coefficients.<sup>23</sup> These properties were exploited in surface acoustic wave devices, infrared sensors, terahertz generators, electro-optic waveguides, etc. Based on the crystallite size and surface area, pyroelectrocatalytic disinfection in LiTaO<sub>3</sub> nano/micro-crystals has also been demonstrated in a recent report.<sup>24</sup>

In this communication, we report the synthesis of LiTaO<sub>3</sub> nanorods by a molten-salt reaction route in which KCl serves as a flux. In a typical synthesis, Li<sub>2</sub>CO<sub>3</sub> (S.D. Fine Chemical, 99.9%), Ta<sub>2</sub>O<sub>5</sub> (Aldrich, 99.99%) and KCl (Merck, 99.9%) were mixed thoroughly in a 1:1:20 molar ratio. A batch of 5g by weight was loaded into a pre-heated furnace (Lenton) at 850°C and maintained at the same temperature for 15 min before quenching to room temperature. The product was then washed with warm double-distilled water thrice after stirring for 30 min each time to remove the chlorides. The structure and morphology of the as-prepared sample were characterized by X-ray diffraction (XRD, PANalytical X'pert Pro), Raman spectroscopy (WiTec Alpha 300), scanning electron microscopy (SEM, Inspect F50 FEI) and high resolution transmission electron microscopy (HRTEM, JEOL 2100F). UV-Vis spectrophotometry (Perkin-Elmer Lambda 750) was employed to obtain the UV-Vis diffused reflectance spectra. Piezo-force microscopic studies were carried out by using a Dimension Icon atomic force microscope (Bruker AXS GmbH). Nd-YAG laser (Spectra-Physics) operating at 1064 nm in Q-switch mode producing 10 ns pulses at 10 Hz was used for second harmonic studies. The output second harmonic intensity

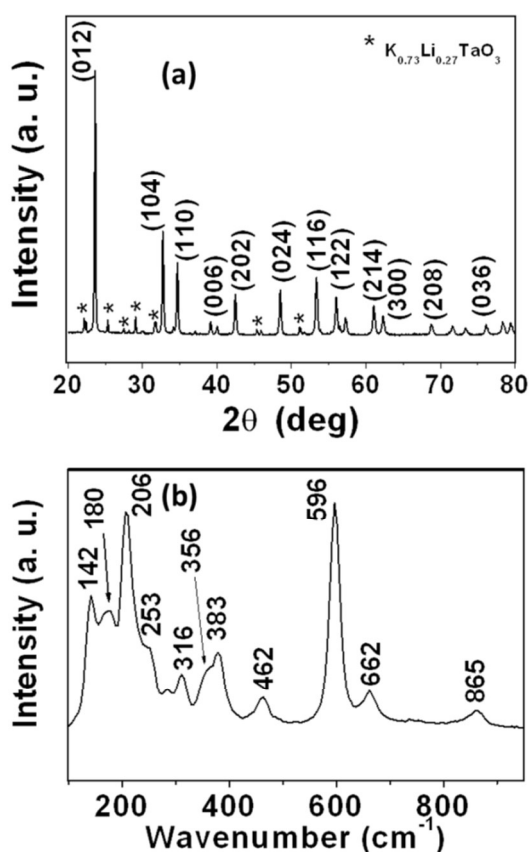


Fig. 1. (a) XRD pattern and (b) Raman spectrum of the as-prepared  $\text{LiTaO}_3$  nanorods.

was recorded with a photomultiplier tube in conjunction with a monochromator.

The XRD pattern obtained for the as-prepared sample is shown in Fig. 1(a). The Bragg peaks match closely with that of the polycrystalline pattern of  $\text{LiTaO}_3$  (ICSD no. 9537). The peaks obtained are indexed to the  $R3c$  space group of  $\text{LiTaO}_3$ , associated with the lattice parameters  $a = 5.137 \text{ \AA}$  and  $c = 13.135 \text{ \AA}$ . A small amount of an impurity phase of  $\text{K}_{0.73}\text{Li}_{0.27}\text{TaO}_3$  (indicated by \* in Fig. 1(a)) was also observed. Calcination conditions were optimized to obtain single crystalline nanorods, as high heat-treatment temperatures and a high molar ratio of KCl led to high concentrations of the impurity phase. However, at lower calcination temperatures and lower molar ratio of KCl, more of cubic particles rather than anisotropic crystallites were obtained. It is also to be noted that higher heating rate and quenching to room temperature are critical in the formation of the single crystalline nanorods. The effect of heating and quenching rate is discussed in the subsequent section. The Raman spectrum (Fig. 1(b)) recorded for the as-synthesized product corroborates the structural units present in the system. The ten major Raman peaks are indexed. The peaks at 142, 180, 206, 316, 383, 462, 662 and  $865 \text{ cm}^{-1}$  correspond to E modes, whereas  $A_1$  vibration modes (transverse optical modes) are characterized by the peaks at 253, 356 and  $596 \text{ cm}^{-1}$ .<sup>25–27</sup> The  $A_1$  mode at  $596 \text{ cm}^{-1}$  is attributed to Ta–O

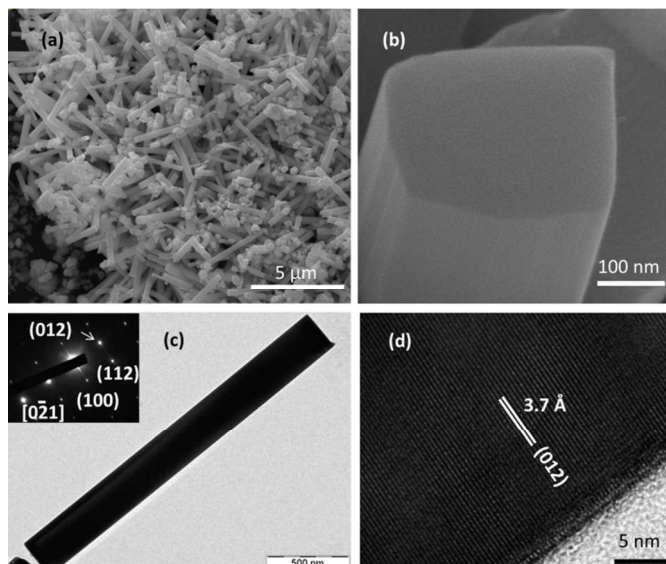


Fig. 2. (a) and (b) SEM; (c) TEM (with SAED pattern in the inset); and (d) HRTEM images of the as-prepared  $\text{LiTaO}_3$  nanorods.

stretching involving the oxygen atoms, whereas those at 253 and  $356 \text{ cm}^{-1}$  are attributed to Li–O framework and oxygen octahedral, respectively. The peak at  $462 \text{ cm}^{-1}$  (E mode) is due to Ta–O bending.

A high yield of  $\text{LiTaO}_3$  nanorods is confirmed based on the SEM images as presented in Fig. 2(a). The as-obtained nanorods maintain an average width of 300 nm and a length of 3  $\mu\text{m}$  (depicted in Fig. S1). The SEM images show an agglomeration of nanorods, with small cubic particles adhering to the large nanorod crystallites. A closer examination of the morphology of the nanorods (Fig. 2(b)) suggests that these are smooth and faceted with a rectangular cross-section. A further insight into the microstructure of the nanorods was obtained by TEM imaging. The bright field TEM image shown in Fig. 2(c) depicts a nanorod of around 300 nm in width and 2  $\mu\text{m}$  in length. The selected area electron diffraction pattern (shown as inset in Fig. 2(c)) confirms the single-crystalline nature of the nanorod and is recorded along  $[0\bar{2}1]$  zone axis. The high crystallinity of the product is confirmed by HRTEM (Fig. 2(d)). The  $d$ -spacing associated with the distinct lattice fringes in the HRTEM image is 3.7  $\text{\AA}$ . This corresponds to the (012) planes of  $\text{LiTaO}_3$ , indicating a preferential growth along that plane. In order to understand the influence of heating and quenching rates on the nanorod formation, SEM analysis on the reaction products that are obtained from three different heating and cooling rates were performed (Fig. S2). To begin with, a  $3^\circ\text{C}/\text{min}$  heating and cooling rates were maintained and the SEM images showed cubic crystallites with an average size of  $\sim 450 \text{ nm}$  (Fig. S2(a)). Symptoms of nanorod formation were observed under heating and cooling rates of  $40^\circ\text{C}/\text{min}$ , as shown in Fig. S2(b). But when the precursors were subjected to a pre-heated furnace at  $850^\circ\text{C}$ , a high yield of nanorods with uniform dimensions was obtained (Fig. S2(c)). These observations reveal that high heating rate results in the rapid growth along the (012) plane (minimum surface energy) as

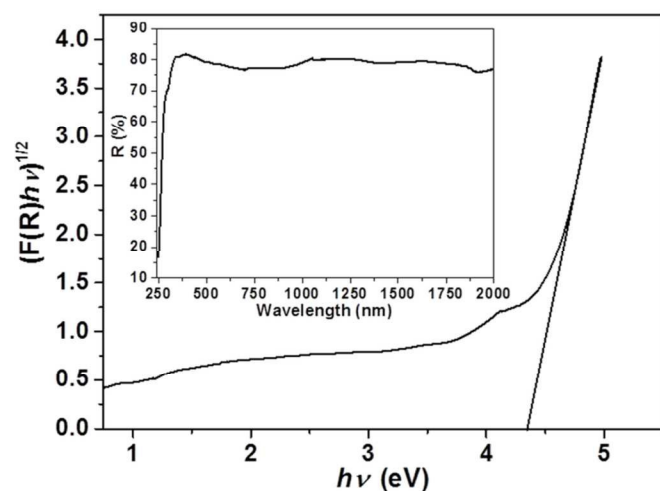


Fig. 3. UV-Vis diffused reflectance spectrum of LiTaO<sub>3</sub> nanorods.

compared to the growth along the other planes and hence yielded anisotropic crystallites. To realize the influence of the molten salt on anisotropic growth of the crystallites, a higher molar ratio of KCl (1:1:35::Li<sub>2</sub>CO<sub>3</sub>:Ta<sub>2</sub>O<sub>5</sub>:KCl) was employed and calcined in a pre-heated furnace at 850°C for 15 min. The SEM images show highly anisotropic crystallites with an average length of 30 μm and thickness of 1–2 μm (Fig. S3(a)) suggesting that the higher salt content increased the diffusion rate of the reactive species resulting in relatively higher aspect ratios. But, unfortunately, the product was accompanied by high content of the impurity phase (Fig. S3(b)).

Diffused reflectance spectrum (shown in the inset of Fig. 3) of LiTaO<sub>3</sub> nanorods was recorded in the 250–2000 nm wavelength range. The reflectance spectrum shows a sharp cut of around 350 nm. Kubelka-Munk function ( $F(R_{\infty})$ ) was invoked in order to relate the diffused reflectance ( $R_{\infty}$ ) emanating from an infinitely thick sample and its absorption ( $K$ ) and scattering coefficients ( $S$ ), which is given by<sup>28</sup>

$$F(R_{\infty}) = \frac{(1-R_{\infty})^2}{2R_{\infty}} = \frac{K}{S} \quad (1)$$

The absorption coefficient ( $\alpha$ ) and the optical band-gap ( $E_g$ ) are related by the Tauc function,<sup>29</sup> which is given by  $ahv = \text{const.}(hv-E_g)^n$ , where  $n = 2$  for an indirect band-gap material. The Tauc and Kubelka-Munk functions can then be equated to determine the optical band-gap by the following expression, considering the scattering coefficient to be constant with the wavelength of light,

$$[F(R_{\infty})hv]^{1/2} = \text{const.}(hv - E_g) \quad (2)$$

The plot of  $(F(R_{\infty})hv)^{1/2}$  vs  $hv$  is depicted in Fig. 3, in which the  $x$ -intercept of a straight line fit along the linear portion of the curve determines the optical band-gap of the material. The calculated band-gap was 4.4 eV, which is close to the 4.6 eV reported for a bulk single crystal.<sup>30</sup> Wave-guiding properties of LiNbO<sub>3</sub> nanowires<sup>31</sup> have been previously demonstrated at different wavelengths of light. The bandgap associated with

these LiTaO<sub>3</sub> nanorods provides another platform to exploit them for wave-guide applications and could probably be used for a relatively wider range of wavelengths.

Piezo-force microscopy (PFM) was employed to investigate into the piezoelectric and ferroelectric properties of the LiTaO<sub>3</sub> nanorods. A schematic of the PFM setup is shown in Fig. 4(a). A small amount of the as-prepared powder was dispersed in ethanol and ultrasonicated for 30 min before depositing on a Pt-coated Si substrate. The substrate was then annealed at 400°C for 1 h to ensure better adhesion of the nanorods to the electrode surface. A conducting Pt-coated Si tip (μmasch) was used as the probe with a tip radius of <40 nm, and a force constant and resonant frequency of 3.5 N/m and 65 kHz, respectively. The piezoelectric vibrations were induced by an ac field of 5 V ( $V_{\text{rms}}$ ) operating at a frequency of 60 kHz.

A 3-D image of the nanorod deposited on the Pt-coated surface is shown in Fig. 4(b). The corresponding amplitude and the phase images are presented in Figs. 4(c) and (d), respectively. The piezoelectric activity in the nanorod is obtained from the amplitude image, whereas the phase image depicts the polarization state of the system and in this case, the piezoelectricity is measured in the direction perpendicular to (012) planes of LiTaO<sub>3</sub> nanorods. Multi-domain structures were observed in the region of interest with the antiparallel domains represented by arrows in Fig. 4(d). Irregularly shaped domains with a width of less than 90 nm are observed. Factors such as crystal facets, tilting of the nanorod relative to the substrate or ineffective contact of the tip on the crystal may affect the piezoelectricity observed in the system. The phase curve (Fig. 4(e)) is characteristic of a ferroelectric hysteresis loop, recorded under a dc bias of –12 to +12 V, whereas the amplitude curve (Fig. 4(f)) is representative of a typical strain-electric field “butterfly loop”. The asymmetry in the loop is attributed to polarization pinning owing to an internal built-in potential or space charge effect.<sup>32</sup>

The applied voltage ( $V$ ) and the associated displacement ( $D$ ) are related by the equation<sup>11,33</sup>

$$(D - D_1) = d_{33}(V - V_1) \quad (3)$$

where  $D_1$  and  $V_1$  are the displacement and applied voltage at the intersection, respectively, and  $d_{33}$  is the effective piezoelectric coefficient. A piezoelectric hysteresis loop ( $d_{33}$ - $V$ , as shown in Fig. 4(f)) can, thus, be obtained from the above equation and an estimated piezoelectric coefficient is in the range of 4–8 pm/V.

In addition to piezoelectricity, the non-linear optical properties (second harmonic generation) of the nanorods were also investigated. The schematic sketch of the experimental setup is displayed in Fig. 5(a). Cubic particles (with an average crystallite size of 1 μm) of LiTaO<sub>3</sub> were also studied in order to compare the effect of anisotropy of crystallites on the second harmonic efficiency. The sample, in the form of powder, was packed between grooved thin glass slides. A fundamental wavelength of 1064 nm was incident on the sample resulting in a second harmonic at 532 nm.

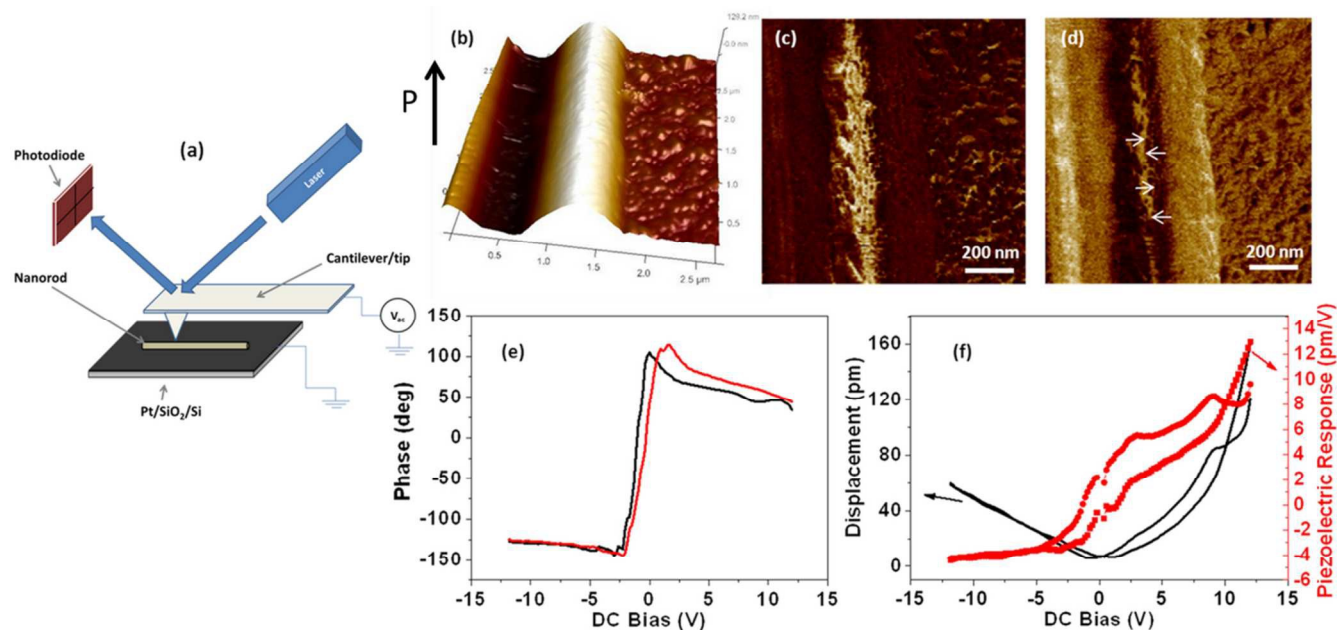


Fig. 4. (a) Schematic of the PFM set-up; (b) 3-D PFM image of an individual LiTaO<sub>3</sub> nanorod; (c) amplitude and (d) phase images of the nanorod; (e) phase curve and (f) local displacement–voltage loop and piezoelectric response hysteresis loop obtained from the LiTaO<sub>3</sub> nanorod.

A 532 nm mirror was used to collect the second harmonic light which was then focused on to the photodetector by a convex lens.

The samples were angle tuned for obtaining the maximum intensity. The intensity profile at 532 nm for the nanorods and cubic crystallites for an incident wave with a power of 1 W are shown in Fig. 5(b). An enhancement in the second harmonic intensity of nearly 1.4 times was observed for the nanorods compared to the cubic crystallites for the same input intensity. Also, the second harmonic intensity emanating from the nanorods was around 0.4 times that of intensity obtained with respect to the first intense peak obtained on rotating (001) face of a KDP single-crystal of 0.65 mm thickness. A polarization anisotropy is induced in 1-D structures due to a large dielectric constant contrast between the crystallites and the surroundings.<sup>34,35</sup> The attenuation in the induced electric field of the anisotropic crystallites for an incident beam polarized perpendicular to the nanowires/rods causes a polarization anisotropy, however the parallel polarization does not induce any changes. This may have led to the enhanced second harmonic conversion efficiency in a randomly packed one-dimensional nanocrystallites compared to the cubic single crystallites since the latter displays no polarization anisotropy. Fig. 5(c) depicts second harmonic intensity as a function of incident light intensity for LiTaO<sub>3</sub> nanorod and cubic crystallites. The collective SHG intensity ( $I_{2\omega}$ ) emanating from nanoparticles in a focal volume is related to the incident light intensity ( $I_{\omega}^2$ ) by the following equation,<sup>36,37</sup>

$$I_{2\omega} \propto n^2 \langle \beta^2 \rangle I_{\omega}^2 \quad (4)$$

where  $n$  is the number of unit cells in the illuminated volume and  $\beta$  corresponds to the non-linear optical susceptibility

coefficient of the system. The second harmonic intensity arises as a consequence of the sum of all the induced dipole moments in the illuminated volume. A satisfying fit, based on the above equation, between the second harmonic and the fundamental intensity has been observed.

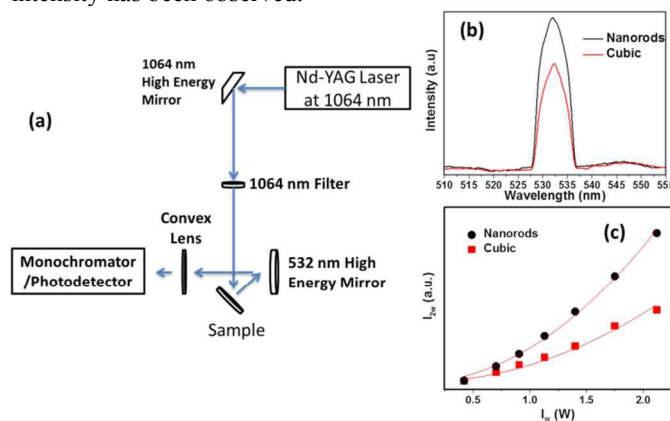


Fig. 5 (a) Schematic of the experimental set-up to probe SHG in LiTaO<sub>3</sub> nanorods, (b) SHG intensity at 532 nm, (c) SHG intensity (at 532 nm) as a function of input intensity of fundamental light for nanorods and cubic particles.

## Conclusions

Single crystalline LiTaO<sub>3</sub> nanorods of dimensions 300 nm in diameter and 3 μm in length were produced by a simple molten-salt synthesis. The preferred growth direction of the single crystals was found to be normal to the (012) planes. A maximum piezoelectric coefficient of 8 pm/V was obtained by PFM method. The anisotropic nature of the nanorods of LiTaO<sub>3</sub> reflected in exhibiting higher SHG intensity than that of cubic crystallites. These nanostructures can be exploited efficiently in energy harvesting and opto-electronic applications.

## Acknowledgement

The authors acknowledge Prof. K.K. Nanda for his support in carrying out Raman studies and S.P. Chiniwar for PFM measurements.

## Notes and References

\*Author for communication

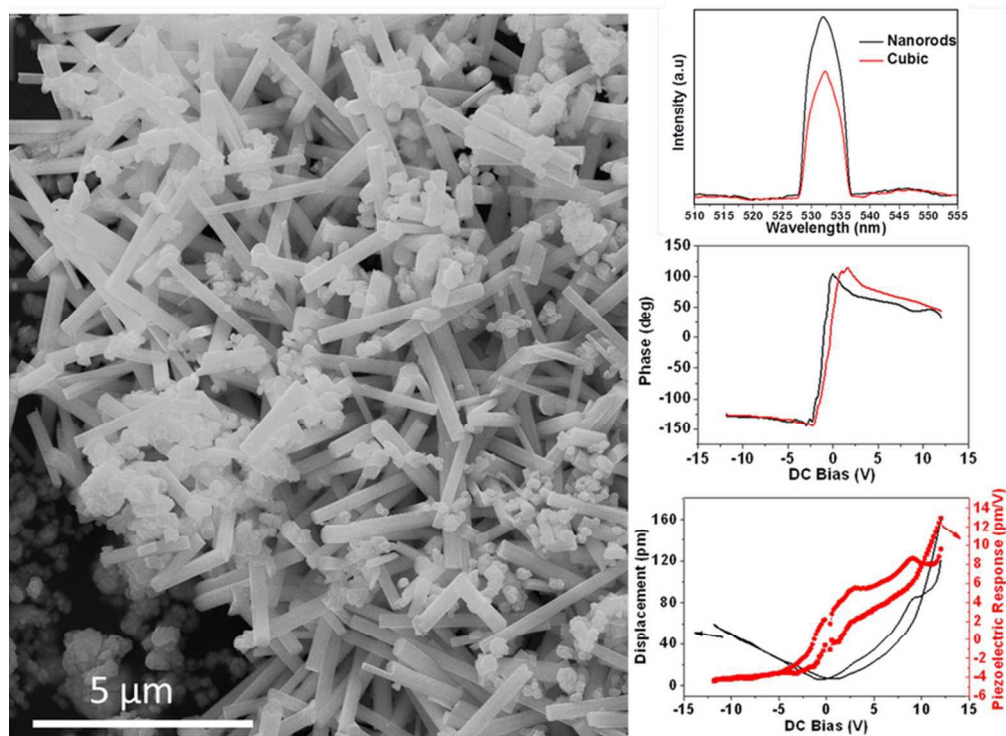
Materials Research Centre, Indian Institute of Science, Bangalore-560012, India.

E-mail: kbrvarma@mrc.iisc.ernet.in;

Fax: +91 80 2360 0683; Tel: +91 080 2293 2914.

† Electronic Supplementary Information (ESI) available: See DOI: 10.1039/c000000x/

- (1) G. Shen, P.C. Chen, K. Ryu and C. Zhou, *J. Mater. Chem.*, 2009, **19**, 828.
- (2) X.J. Huang and Y.K. Choi, *Sens. Actuators, B*, 2007, **122**, 659.
- (3) B. Tian, X. Zheng, T.J. Kempa, Y. Fang, N. Yu, G. Yu, J. Huang and C.M. Lieber, *Nature Lett.*, 2007, **449**, 885.
- (4) X. Wang, J. Zhou, J. Song, J. Liu, N. Xu, and Z.L. Wang, *Nano Lett.*, 2006, **6**, 2768.
- (5) R.S. Chen, C.A. Chen, H.Y. Tsai, W.C. Wang, and Y.S. Huang, *J. Phys. Chem. C*, 2012, **116**, 4267.
- (6) Z. Liu, J. Xu, D. Chen and G. Shen, *Chem. Soc. Rev.*, 2015, **44**, 161.
- (7) K.I. Park, S.B. Bae, S.H. Yang, H.I. Lee, K. Lee and S.J. Lee, *Nanoscale*, 2014, **6**, 8962.
- (8) Y. Xia, P. Yang, Y. Sun, Y. Wu, B. Mayers, B. Gates, Y. Yin, F. Kim and H. Yan, *Adv. Mater.*, 2003, **15**, 353.
- (9) N. Nuraje and K. Su, *Nanoscale*, 2013, **5**, 8752.
- (10) Y. Mao, T.J. Parka and S.S. Wong, *Chem. Commun.*, 2005, **46**, 5721.
- (11) Z. Chen, J. Huang, Y. Yang, Y. Wang, Y. Wu, H. He, X. Wei, Z. Ye, H. Zeng, H. Cong and Z. Jiang, *RSC Adv.*, 2012, **2**, 7380.
- (12) L.Q. Cheng, K. Wang, Q. Yu and J.F. Li, *J. Mater. Chem. C*, 2014, **2**, 1519.
- (13) B. Liu, B. Hu and Z. Du, *Chem. Commun.*, 2011, **47**, 8166.
- (14) S. Nah, Y.H. Kuo, F. Chen, J. Park, R. Sinclair and A.M. Lindenberg, *Nano Lett.*, 2014, **14**, 4322.
- (15) Y.M. Hu, H.S. Gu, D. Zhou, Z. Wang, H.L.W. Chan and Y. Wang, *J. Am. Ceram. Soc.*, 2010, **93**, 609.
- (16) U.A. Joshi and J.S. Lee, *Small*, 2005, **1**, 1172.
- (17) J. Huang, Z. Chen, Z. Zhang, C. Zhu, H. He, Z. Ye, G. Qu, and L. Tong, *Appl. Phys. Lett.*, 2011, **98**, 093102.
- (18) G. Wang, S.M. Selbach, Y. Yu, X. Zhang, T. Grandea and M.A. Einarsrud, *CrystEngComm*, 2009, **11**, 1958.
- (19) T. Yamada, H. Iwasaki, N. Niizeki, *Jpn. J. Appl. Phys.*, 1969, **8**, 9.
- (20) R. Vaish, *Int. J. Appl. Ceram. Technol.*, 2012, **9**, 1.
- (21) V. Gopalan and M.C. Gupta, *Appl. Phys. Lett.*, 1996, **68**, 888.
- (22) R.C. Miller and A. Savage, *Appl. Phys. Lett.*, 1966, **9**, 169.
- (23) T. Yuhara, K. Tada, and Y.S. Li, *J. Appl. Phys.*, 1992, **71**, 3965.
- (24) E. Gutmann, A. Benke, K. Gerth, H. Böttcher, E. Mehner, *J. Phys. Chem. C*, 2012, **116**, 5383.
- (25) I.P. Kaminov and W.D. Johnston, *Phys. Rev. B.*, 1967, **160**, 3.
- (26) R. Constantine, *Phys. Rev. B*, 1988, **38**, 14.
- (27) Y. Repelin, E. Husson, F. Bennani and C. Proust, *J. Phys. Chem. Solids*, 1999, **60**, 819.
- (28) P. Kubelka, *J. Opt. Soc. Am.*, 1948, **38**, 448.
- (29) J. Tauc, *Optical Properties of Non-Crystalline Solids*, F. Abele's edn., North-Holland Publishing Co., Amsterdam, 1972.
- (30) E.J. Guo, J. Xing, H.B. Lu, K.J. Jin, J. Wen and G.Z. Yang, *J. Phys. D: Appl. Phys.*, 2010, **43**, 015402.
- (31) J. Huang, Z. Chen, Z. Zhang, C. Zhu, H. He, Z. Ye, G. Qu and L. Tong, *Appl. Phys. Lett.*, 2011, **98**, 093102.
- (32) A. Gruverman, B. J. Rodriguez, A. I. Kingon, R. J. Nemanich, J. S. Cross, and M. Tsukada, *Appl. Phys. Lett.*, 2003, **82**, 3071.
- (33) Y.C. Yang, C. Song, X.H. Wang, F. Zeng and F. Pan, *Appl. Phys. Lett.*, 2008, **92**, 012907.
- (34) J. Wang, M. S. Gudiksen, X. Duan, Y. Cui and C. M. Lieber, *Science*, 2001, **293**, 1455.
- (35) R. Grange, J-W. Choi, C.L. Hsieh, Y. Pu, A. Magrez, R. Smajda, L. Forró and D. Psaltis, *Appl. Phys. Lett.*, 2009, **95**, 143105.
- (36) D. Isakov, E.M. Gomes, M.S. Belsley, B. Almeida and N. Cerca, *Nanoscale*, 2012, **4**, 4978.
- (37) S. Brasselet and J. Zyss, *C. R. Phys.*, 2007, **8**, 165.



Second Harmonic Generation and Piezoelectric response from  $\text{LiTaO}_3$  nanorods.  
73x54mm (300 x 300 DPI)